Chapter 8

MIMO Actuator Force Control of a Parallel Robot for Ankle Rehabilitation

This chapter presents a multi-input multi-output (MIMO) force controller for a parallel robot that is used for ankle rehabilitation. The robotic device is an advanced rehabilitation system compared to current designs through modeling the patient's ankle as part of the robot in the kinematic design. The MIMO actuator force controller is designed so that the gains along the decoupled directions can be pushed closer to their corresponding gain margins to enhance force-tracking performance over uniform gain approaches. The force controller will be used in the loop to provide an adaptive interaction control to perform repeatable and objective physiotherapy to patients following an ankle injury.

8.1. Introduction

While robots have long been used for automation of industrial processes, there is a growing trend where robotic devices are used to provide services for end users. An area where robots are believed to have a significant impact is healthcare. Accessibility to healthcare services is a vital component to improve the quality of life. However, the trend of aging populations will certainly increase demand on healthcare and create more strain on the already

---

Chapter written by Andrew MCDAID, Yun HO TSOI and Shengquan XIE.

limited resources available. For this reason, much research has been dedicated to medical and healthcare robots.

8.1.1. *Rehabilitation robots*

Robots have been used for rehabilitation purposes since the 1960s [HAR 95]. The application of robots in rehabilitation was initially more focused on replacing lost functions in individuals with physical disabilities through the use of devices such as robotic orthoses, robotic workstations, feeding devices and robotic wheelchairs [TEJ 00]. Over the last two decades, however, with major advances in mechatronics engineering [HAB 06, HAB 08], there has been an increasing amount of research into the use of robots in physical therapy. One of the main motivations behind the adoption of robots in physical therapy is the potential improvement in productivity [KRE 00]. Physical therapy normally requires manual manipulation of the patient's affected limb, and these manipulations can be rather labor intensive. Consequently, such rehabilitation exercises can easily lead to the onset of fatigue in the therapist, thus limiting the duration and intensity of the therapy session. Since robots are well suited for repetitive tasks and can be designed to have adequate force capabilities, their use in the execution of these exercises will be able to reduce the physical workload of therapists, and can potentially allow the therapists to simultaneously oversee the treatment of multiple patients in a supervisory role [KRE 00, RIE 05].

The use of robots in physical therapy also provides further advantages due to their high repeatability and ability to collect a vast amount of quantitative data when equipped with appropriate sensors. Since therapists mainly operate on the basis of their "feel", their evaluation of the patient's condition can be subjective. By using robotic devices, diagnosis and prognosis can be made more objectively using quantitative data, and comparisons between different cases can also be made more easily [RIE 05]. The high repeatability of the robotic devices also allows therapy to be applied more consistently and will help to identify the effectiveness of the treatment. As a result, in addition to the delivery of physical therapy, robots can also contribute to rehabilitation research.

Existing robots designed for physical therapy are commonly involved with neuromotor training of patients suffering from neurological disorders [HES 03, REI 04]. Robots used in this capacity are generally required to manipulate the patient's affected limb by guiding it along certain motion trajectories. It can be seen that rehabilitation robots share several common

traits. The obvious feature found in all these robots is the emphasis on the user's safety. As the patient is tightly coupled to the rehabilitation robot during its operation, it is vital that the patient–robot interaction forces or torques be maintained at safe levels to prevent any injuries. Therefore, this requires the robotic devices to have some degree of compliance or in other words, to be backdrivable. Inherent backdrivability can be realized by using a low actuator transmission ratio or by decoupling the actuator mass from its end point through the use of elastic elements. Alternatively, force feedback control can be used to reduce the apparent actuator mass and improve the backdrivability of actuators [HOG 87, HOG 05].

Physical characteristics such as size, shape, mass, joint kinematics, motion range and joint dynamics can vary considerably among individuals. Robots designed for rehabilitation must therefore be adjustable or adaptable so that they can cater for a larger population. If these characteristics are not taken into consideration in the robot controller, the robot may become unstable or it may apply excessive forces in non-compliant directions, thus presenting a dangerous scenario for the patient.

Another common feature among rehabilitation robots is the need to control the physical interaction between the patient and the robot. This means that both the motion of the robot and the contact forces applied to the patient must be regulated. Motion regulation is generally required when guiding the patient's limb along paths that are representative of reaching tasks for the upper limb or trajectories which corresponds to normal gait pattern for the lower limb. The requirement to control forces and torques, on the other hand, can arise from concerns of the patient's safety or from the need to apply resistive effort for strength training exercises.

8.1.2. *Ankle sprain rehabilitation*

Ankle sprains are injuries that involve the overstretching of ligaments around the ankle and are often sustained during sporting or physical activities. Due to its location, the human ankle is frequently subjected to large loads, which can reach up to several times the body weight. The exposure to such large loads also means a higher likelihood of injuries. In fact, the ankle is the most common site of sprain injuries in the human body, with over 23,000 cases per day in the United States [HER 02]. In New Zealand, approximately 82,000 new claims related to ankle injuries were made to the Accident Compensation Corporation (ACC) in the year 2000/2001, costing

an estimated 19 million NZD and making ankle-related claims the fourth biggest cost for ACC [ACC 07].

Depending on the severity of the sprain, the time required for recovery can range from 12 days to more than six weeks [SAF 99]. Researchers have reported that a significant number (>40%) of severe ankle sprains can develop into chronic ankle instability [SAF 99], which makes the ankle more susceptible to further injuries in the future. Chronic ankle instability is thought to be caused by a combination of mechanical and functional instabilities at the ankle. Mechanical instability refers to changes of the ankle anatomy that makes it more prone to future sprain injuries, whereas functional instability refers to changes that give rise to insufficiencies in the ankle neuromuscular system, such as impaired proprioception, muscle weakness and reduced neuromuscular control [HER 02].

The general rehabilitation program for ankle sprains is carried out in stages. The initial stage of treatment right after injury is focused on reducing effusion and swelling at the affected area to promote healing of the injured tissues. A reduction in effusion can be achieved with elevation, application of ice and compression. The affected ankle is also often immobilized. However, as prolonged immobilization of the ankle can lead to a reduced range of motion (ROM) and muscular atrophy, the next phase of ankle rehabilitation typically involves ROM and muscle strengthening exercises. Once effusion has stopped, active and passive ROM exercises are normally carried out within the pain-free range of the patient. Research suggests that this has the ability to stimulate healing of torn ligaments [SAF 99]. Once pain-free weightbearing gait is achieved, muscle stretching and resistive exercises can be initiated, where the resistance level should be increased as the patient progresses with recovery. Muscle stretching is important to assist the recovery of joint ROM while resistance training is used to improve the strength of muscles surrounding the ankle to prevent future injuries [MAT 02]. Finally, proprioceptive and balancing exercises should be carried out toward the end of the rehabilitation program to enhance the patients' sense of joint position, thus giving them better foot and ankle coordination and improving their ability to respond to sudden perturbations at the ankle [SAF 99].

As can be seen from the previous discussion, muscular strength and good proprioception are vital in preventing functional instability of the ankle. Therefore, emphasis must be given to these areas and an extensive rehabilitation program is needed to minimize the likelihood of recurrent injuries. The repetitive and tedious nature of such exercises, therefore, makes

robotic devices an attractive alternative to manual manipulation. Various robotic platforms have therefore been developed for the rehabilitation of ankle injuries to reduce the physical workload of therapists and supplement the resources required to facilitate a comprehensive rehabilitation regime so that adequate therapy can be delivered to the patients. However, further development is still required to enhance the adaptability and to improve the suitability of existing devices as clinical measurement tools.

8.2. Ankle rehabilitation robot

Due to the high incidence and potentially lengthy rehabilitation period of ankle injuries, there is a significant demand for the treatment of such injuries. As physical therapy is vital in the promotion of recovery and prevention of future injuries, effort is required to ensure the availability of this service. Introduction of robots in ankle rehabilitation will allow delegation of tedious rehabilitation tasks to the robot, and allows therapists to extend care to more patients. As discussed previously, robots can also be used as evaluation tools to determine the progress and capability of the patients. This means that robots can potentially be used to determine whether a patient has achieved a suitable level of muscle strength and proprioceptive capability required to prevent future injuries.

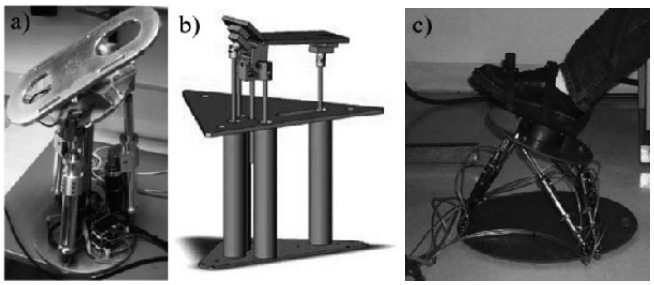

Figure 8.1. *Examples of platform based ankle rehabilitation robots. a) The ankle exerciser developed in [BON 07]; b) the reconfigurable ankle rehabilitation robot developed in [BUF 08]; c) the Rutgers ankle rehabilitation interface developed in [YAG 04] (Images reproduced from [ROY 07], [YOO 05] and [TRU 10])*

A range of platform-based devices have been developed by researchers for the purpose of sprained ankle rehabilitation [GIR 01, YOO 05, LIU 06, YOO 06, SYR 08, SAG 09], some of which are shown in Figure 8.1. They are designed to carry out various ankle rehabilitation exercises such as

motion therapy and muscle strength training. Motion therapy can be divided into passive, active-assist and active exercises, each requiring a different level of participation from the patient, ranging from no active effort in the passive exercises to full user-driven motion in active exercises. Strength training, on the other hand, requires the robot to apply a resistive load to impede the user's movement to improve muscle strength.

A survey of existing ankle rehabilitation robots shows that the end-effectors of existing platform-based systems are typically constrained about a center of rotation that does not coincide with the actual ankle joint [YOO 05, LIU 06, YOO 06, SAG 10]. A result of this is that the user's shank will not be stationary during operation of these robots if the natural ankle–foot motion is to be maintained. Consequently, orientation and interaction moments of the robotic platform are unlikely to be equivalent to the actual displacement and moments found between the foot and the shank. Therefore, this makes these existing devices less suitable for evaluation purposes due to the greater uncertainties in the motion/force information.

Different actuators were used in platform-based ankle rehabilitation robots. The Stewart platform-based device in [GIR 01] and the reconfigurable ankle rehabilitation platform in [YOO 05, YOO 06] have utilized pneumatic cylinders to provide actuation, while electric motors were used in devices developed in [LIU 06, SUN 07, LIN 08]. A custom-designed electric actuator was proposed in [SAG 09, SAG 10] to improve actuator backdrivability, whereby a cable-driven pulley system is used to convert the rotational motion of a direct current (DC) motor into linear motion of the actuator rod.

8.2.1. *Design requirements*

To carry out different ankle rehabilitation exercises, the robot to be developed must have a workspace similar to or more than the typical range of motion encountered at the human ankle. The ankle–foot motion is primarily rotational and is often described by rotations on three mutually perpendicular anatomical planes. These rotations are illustrated in Figure 8.2. The plane that distinguishes the left and right sides of the body is called the sagittal plane. The frontal plane, as its name suggests, divides the body into front and back halves. Finally, the transverse plane divides the body into top and bottom portions. Rotational motion of the foot on the sagittal plane is called plantar flexion, which happens when the toes are pushed further away from the head, and rotational motion of the foot in the opposite direction is called dorsiflexion. Inversion is used to describe the rotation of the foot on the

frontal plane where the inner or medial side of the foot is raised upward, with eversion being its complementary motion. Finally, internal rotation or adduction is used to describe the rotational motion on the transverse plane which moves the toes toward the center of the body, whereas the movement in the opposite direction is called external rotation or abduction. The typical motion limits along these different directions as determined in an *in vitro* study by Siegler *et al.* [SIE 88] are shown in Table 8.1.

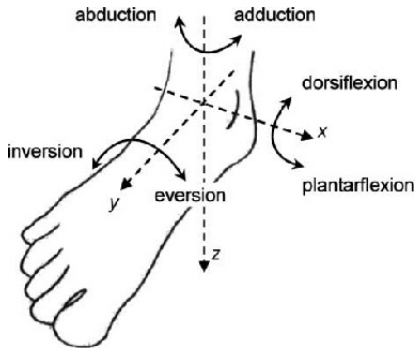

Figure 8.2. *Rotational motions of the human ankle*

Type of motion	Maximum allowable motion		
	Range (deg)	Mean (deg)	Standard deviation (deg)
Dorsiflexion	20.3–29.8	24.68	3.25
Plantar flexion	37.6–45.75	40.92	4.32
Inversion	14.5–22	16.29	3.88
Eversion	10–17	15.87	4.45
Internal rotation	22–36	29.83	7.56
External rotation	15.4–25.9	22.03	5.99

Table 8.1. *Typical range of motion at the human ankle [SIE 88]*

It can be seen that the extents of motion available in different directions are quite different and the overall ankle range of motion is small. It should be noted that since the robot should be able to cater for both the left and right legs, the different motion limits in the inversion–eversion and internal–external rotation directions will be inverted in the robot coordinate frame

when a foot from the different side of the body is placed on the robot. The limits of the required robot rotational workspace on the frontal and transverse planes are therefore symmetric.

Another quantity that has a significant influence on the design of the ankle rehabilitation robot is the level of moment that the ankle–foot structure is expected to experience during rehabilitation. In terms of the maximum moment required at the plantar-/dorsiflexion motion, results from an *in vivo* study in [KEA 90] confirm that a maximum range of 71.7 Nm is required to move the foot of the subject passively from the maximum plantar flexion to the maximum dorsiflexion. The same study also evaluated the torques produced by maximum voluntary contraction of the subjects and the corresponding values for dorsiflexion and plantar flexion are 54.4 Nm and 126.0 Nm, respectively. Similar results in terms of passive ankle moments were also observed in an *in vitro* study by Paranteau *et al.* [PAR 98], which gives a maximum dorsiflexion moment as –44 Nm and a maximum plantar flexion moment of about 37 Nm. Maximum joint torque in the inversion–eversion directions is also available from [PAR 98], where values of 33 Nm in inversion and 44 Nm in eversion were reported. Unfortunately, maximum torque for internal/external rotation is not available from the above studies. The robot used in this research was designed by assuming that the maximum internal/external rotation moments are similar in magnitude to the inversion/eversion moments. In summary, the moment requirements of the ankle rehabilitation robot are set at 100 Nm for moments about the X Euler angle axis, and 40 Nm for the remaining two Euler angles axes.

In terms of functionality, ankle rehabilitation robots will have to be able to accommodate different types of rehabilitation exercises, which include passive, active-assist and active ROM exercises, as well as muscle strengthening routines. Passive ROM exercises will involve the robot guiding the user's foot through its permissible range of motion when the user's foot remains relaxed. Active-assist ROM exercises, on the other hand, require the robot to "cooperate" with the user to perform the required foot motion, providing assistance on an as-needed basis, while active ROM exercises provide full control of the foot motion to the user, with the robot providing minimal interaction forces/moments. As for the realization of muscle strength training exercises, the robot should be able to provide a constant level of resistance to the foot or vary the resistance according to the extent of displacement (i.e. act as an elastic element).

8.2.2. *Analysis for four-link parallel mechanism*

Parallel mechanisms have a kinematic structure whereby the end-effector is connected to a fixed base through multiple actuated links. Due to this arrangement, parallel robots have several advantages over their serial counterparts. One of these advantages is a higher positioning accuracy since errors in the actuated joints no longer accumulate as in the case of serial robots. Furthermore, since the end-effector is supported by multiple actuators, the load capacity of the mechanism can also be increased. As actuators of a parallel robot are located at its base rather than on its moving links, the total load moved by the manipulator is also reduced. As a result, parallel mechanisms can be used to achieve higher bandwidth in motion (e.g. Delta robot).

Due to its many advantages and the relatively large loads experienced at the ankle and foot, parallel mechanisms are excellent candidates for ankle rehabilitation devices. In fact, the human lower leg and foot can itself be viewed as a parallel mechanism with the foot being the end-effector and the muscles spanning across the ankle being the actuating links. From the above discussion, it can be seen that there is sufficient motivation for the use of a parallel robot in this research. The major shortcomings of parallel mechanisms, however, come in the form of a reduced workspace and increased kinematic singularities [TSA 99, MER 06]. Fortunately, as the ROM of the human ankle is limited, the smaller workspace of parallel manipulators may still be adequate, provided that suitable kinematic parameters are selected for the mechanism. However, singularities pose a much greater concern and must be considered in the design of the manipulator.

Due to the incorporation of the human ankle as part of the parallel mechanism, its kinematic description must be established before any analyses on the workspace, singularities and moment capabilities of the ankle rehabilitation robot. Although foot motion is often depicted through rotations about two oblique revolute joints in series [INM 76, DUL 85, SIM 68], its actual movement pattern appears to be more complicated with coupled translations and rotations. Studies found that the orientations of the revolute joints in the biaxial model can vary significantly among individuals. Furthermore, it was also found that such axes orientations also vary with the configuration of the foot. Based on these findings, the generality of results obtained from using a specific biaxial ankle model in the workspace and singularity analysis would be compromised. A natural choice of a kinematic model to replace the biaxial model is a spherical joint as it can cater for all

possible rotational motions. However, this approach still fails to address the effects of translational motion. As the movement of the ankle can be considered primarily rotational with limited translational movement of its instantaneous axis of rotation [YIN 05], analyses that consider the ankle as a spherical joint can still be used to give an indication of the available workspace and singular regions.

After developing a conventional parallel robot mathematical formulation, as per [MIT 03], and carrying out a full design analysis, including the workspace, singular region and actuator force analyses that is presented in [TSO 10], a four-link parallel mechanism was chosen by the authors. The attachment points of the four-link mechanism on the end-effector and the base platform considered in this research share the same parameterization as the three link version. The kinematic structure of the mechanism can therefore be represented by Figure 8.3.

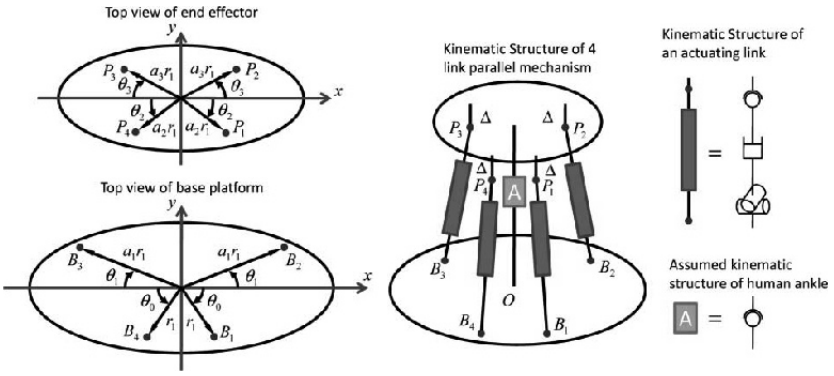

Figure 8.3. *Kinematic structure of the three-link parallel mechanism*

In Figure 8.3, the attachment points of the actuated links on the base are denoted by B_i while their attachments on the end-effector are represented by P_i. Based on the UPS link structure, point B_i is coincident with the center of the universal joint while point P_i is coincident with the center of the spherical joint or equivalent on the *i*th actuated link. Point O had also been defined on the base platform where it acts as the origin of the robot global coordinate frame. The points B_i and O are constrained to lie on the same plane and their relative positions are parameterized in polar coordinates. The projections of points P_i on the end-effector can similarly be represented in polar coordinates. In addition, the distance between P_i and the end-effector plane is

also set to be constant for all i, and is denoted by Δ. Finally, the point A is defined as the center of the spherical joint used to represent the human ankle.

Using the proposed kinematic structure, the end-effector can be seen to pivot about the actual ankle center and not an external point. Consequently, when the shank is fixed on the base platform and the foot is placed on the robot end-effector, the robot would have completely isolated the ankle joint. Motion and moments of the end-effector taken about the ankle center will therefore, respectively, provide accurate indications of the relative orientation and moments between the user's foot and shank.

The workspace and condition numbers for the final design were also computed for different locations of the spherical joint (i.e. OA) to simulate the translation of the actual ankle center of rotation. In the final design analysis, OA was varied within a 30 mm cube centered about its nominal location. However, positions of the end-effector attachment points, $P_{i,o}$, were held constant with respect to the global robot frame. The choice of the 30 mm cube was based on sources in the literature which estimates the range of ankle translation to be between 10 and 20 mm [YIN 05]. It should be noted that the workspace produced from this analysis will also have some safety margin against small deviations in the foot placement location on the robot end-effector. The upper and lower bounds of the actuator lengths used in this analysis also differed slightly with those of the original analysis where actuator length limits are dependent on the actuator lengths at the neutral foot configuration. In the final design, the construction of the actuated links was made to be uniform across all links and they therefore share the same motion limits. Analysis of the reachable workspace had shown that this design decision had the effect of improving the maximum motion allowable in the plantar flexion direction at the expense of smaller dorsiflexion movements. Since the original dorsiflexion motion limit is much more than the natural dorsiflexion motion limit, this design change is not expected to significantly compromise the ability of the proposed robot in meeting the workspace requirements.

The workspace, singular region and actuator force analyses carried out on the four-link mechanism with kinematic parameters are given in Table 8.2 and the results for a slice of the robot workspace are shown in Figure 8.4. The kinematic parameters of this parallel mechanism also appear to be capable of producing a larger robot workspace in the flexion directions, with maximum plantar flexion of about 52° and maximum dorsiflexion of about 48°. The motion limits about the Y-Euler axis, however, was found to

decrease slightly to 34°, but it still satisfies the required range of motion. Finally, the range of Z-Euler rotations in the workspace is also more than adequate to accommodate the natural ankle movements. An inspection of the actuator force requirements also shows that with four actuators, the maximum actuator force exerted to achieve the prescribed task space moment is now reduced to about 1,700 N from over 3,000 N in the three-link mechanism.

Parameter	r_1	a_1	a_2	a_3	θ_0	θ_1	θ_2	θ_3	Δ	$\overrightarrow{OA}$
Value	0.2 m	0.9	0.4	0.45	–45°	45°	–30°	30°	0.05 m	[0 0 0.36] m

Table 8.2. *Kinematic parameters for the four-link parallel mechanism*

Figure 8.4. *The common robot workspace at zero Z-Euler angle. The information shown is for the four-link parallel mechanisms obtained by varying $\overrightarrow{OA}$ within a 30 mm cube centered about its nominal value*

The results obtained from the above analysis show that the estimated range of motion can be considered adequate, with a maximum plantar flexion of 44°, maximum dorsiflexion of 36° and maximum inversion–eversion of 26°. The available abduction and adduction motion again remains large at about 70°. The moment capacity of the final design can also be evaluated by considering the maximum forces available from the actuators. This can be done by considering the maximum moments that can be applied at all

end-effector orientations which belong to the common workspace and taking the smallest of these values. Note that this moment analysis was carried out on each of the X, Y and Z directions by using a maximum actuator force output of 2,000 N. The moment capacity and the maximum achievable end-effector orientations of the final design are summarized in Table 8.3. It can be seen that the movements and moments achievable by the four-link parallel mechanism are similar to what is required for the X and Y directions, and more than what is needed in the Z direction, thus indicating the capability of the proposed structure to perform the required rehabilitation exercises.

Direction	Maximum motion	Moment capacity
Plantar flexion (positive X)	44°	151 Nm
Dorsiflexion (negative X)	36°	151 Nm
Inversion (positive Y)	26°	38 Nm
Eversion (negative Y)	26°	38 Nm
External rotation/Abduction (positive Z)	72°	68 Nm
Internal rotation/Adduction (negative Z)	72°	68 Nm

Table 8.3. *Motion limits and moment capacity of the four-link parallel mechanism*

8.2.3. *System description*

A prototype of the ankle rehabilitation robot had been constructed using the kinematic parameters investigated above. Brushed DC motor-driven linear actuators (Ultra Motion Bug Linear Actuator 5-B.125-DC92_24-4-P-RC4/4) had been used as the actuated prismatic joint in the prototype. The linear actuator was chosen based on the stroke length and force requirements of the mechanism, with an actuator stroke length of 0.1 m, force capacity of over 2,000 N and a top speed of 0.066 m/s. In terms of sensors, linear potentiometers were built into the actuators to provide measurement of the actuator lengths. Additionally, a two-axis inclinometer (Signal Quest SQ-SI2X-360DA) was attached to the end-effector platform to allow the measurement of its pitch and roll angles. Lastly, four tension–compression load cells (Omega Engineering LC201-300) were also installed at the interface between the linear actuator and the effective spherical joints to monitor the forces along the actuated links. The ankle rehabilitation robot developed in this research is shown in Figure 8.5, both in the form of a three-dimensional model and in the form of a photograph depicting how the robot interacts with the user. In terms of controller hardware, an embedded

controller (National Instruments NI-PXI 8106) had been used together with a Data Acquisition (DAQ) card (National Instruments NI-PXI-6229) to carry out the signal processing and execute the real-time control functions of the prototype. The embedded controller was also connected to a *personal computer* to receive user commands and display the sensor measurements through a user interface developed using the LabView programming environment.

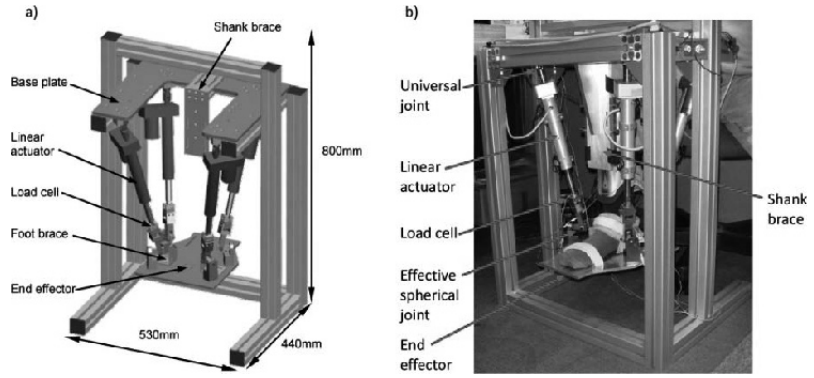

Figure 8.5. *The 3D CAD model of the developed ankle rehabilitation robot a) and a photograph showing the robot with the user's lower limb attached b)*

8.3. Actuator force control

Operation of the rehabilitation robot relies on implementation of a suitable interaction controller, and a force-based control approach has been taken, whereby the desired robot impedance is realized through a MIMO actuator-level force control. Preliminary experimental trials carried out in this research revealed that independent application of actuator force control schemes (as are conventionally implemented) on each actuator yielded undesired oscillatory behavior. Consequently, the MIMO actuator force controller that takes into account the coupling effects introduced by kinematic constraints of the parallel manipulator was used to improve the force control performance.

The design of a force controlled loop has been considered in this research and although various actuator force/torque control techniques are available in the literature [MUR 93, KAT 06, KAT 08, KON 08], they are mainly focused on the control of a single actuator as a single-input single-output (SISO) system, and do not consider the overall kinematics of the mechanism being

driven. These schemes also often require measurements of velocities and good knowledge of the robot dynamics. As significant force coupling can be found among the actuator forces in a parallel robot, independent actuator force control may lead to performance degradation as force interactions between various actuators will simply be treated as additional disturbances in the SISO force controllers. A MIMO approach for actuator force control that takes into account the kinematic and inertial information of the parallel manipulator is presented here.

8.3.1. *Actuator force control by decoupling of inertia matrix*

The dynamics of the actuators used in this research has to be considered to gain a better understanding of the coupling that arises when these actuators are installed on the parallel robot. The equation governing the dynamics of the brushed DC motor-driven linear actuators used in this research is given here [8.1], where $\mathbf{F_{act}}$ is the actuator force resisting the actuator motion, i is the actuator current, I is the actuator length, K_t is the torque constant of the motor, K_a is the transmission ratio between the rotary and linear displacements, J_{eff} is the effective motor rotational inertia, b_{eff} is the effective motor viscous damping coefficient and F_{fric} is the effective Coulomb friction acting on the actuator rod.

$$F_{act} = K_t K_a i - K_a^2 J_{eff} \ddot{l} - K_a^2 b_{eff} l - F_{fric} \qquad [8.1]$$

Provided that the actuators share the same characteristics, equation [8.1] will be equally applicable for the case where the actuators are coupled through a parallel mechanism. In such a scenario, the variables F_{act}, i, l and F_{fric} can simply be treated as vectors. This relationship can, therefore, be integrated with the task space dynamics to give the overall actuator and robot dynamics. As with many manipulators, the robot task space dynamics considered in this chapter can be represented by equation [8.2], where Θ is the task space coordinates in XYZ Euler angles, $M(\Theta)$ is a configuration-dependent inertia matrix, $N(\Theta,\Theta)$ is a vector gathering all the centripetal, Coriolis and gravitational forces, τ_{ext} is the external torque applied to the robot manipulator and J is the manipulator Jacobian. Using this manipulator Jacobian, the task space and joint space velocities and accelerations can also be related through equations [8.3] and [8.4], respectively.

$$M(\ddot{\Theta})\ddot{\Theta} + N(\Theta,\dot{\Theta}) + \tau_{ext} = J^T F_{act} \qquad [8.2]$$

$$\dot{l} = J\dot{\Theta} \qquad [8.3]$$

$$\ddot{l} = J\ddot{\Theta} + J\dot{\Theta} \qquad [8.4]$$

The actuator accelerations can be obtained by substituting the task space accelerations obtained from the rearrangement of equation [8.2] into equation [8.4]. The resulting actuator accelerations and the actuator velocities can then be further incorporated into equation [8.1] to give equation [8.5], where the matrix D is used to describe the coupling between the actuator currents and the resulting actuator forces. The expression for this matrix is given in equation [8.6]. It should be noted that dependencies on the task space coordinates and velocities are dropped hereafter for brevity. Additionally, since the manipulator Jacobian is not square for redundantly actuated robots, the pseudo-inverse (denoted by the operator +) has been used in place of the conventional matrix inverse operation. More specifically, the pseudo-inverse of the manipulator Jacobian is computed using equation [8.7]. It is also worth noting that $J^T(J^+)^T = I$ and $(J^+)^T J^T = I - V_0 V_0^T$, where v_0 is a column-wise collection of the null space vector(s) of J^T.

$$F_{act} = K_t K_a Di + (I - D)(J^+)^T (N + \tau_{ext}) - D\underbrace{[K_a^2 (J_{eff} J + b_{eff} J)\dot{\Theta} - F_{fric}]}_{F_{distb}} \qquad [8.5]$$

$$D = \left(I + K_a^2 J_{eff} J M^{-1} J^T\right)^{-1} \qquad [8.6]$$

$$J^+ = (J^T J)^{-1} J^T \qquad [8.7]$$

Disturbance observer-based controllers have been used by several researchers for position and force control of electric actuators [MUR 93, KEM 99, WAN 04, KAT 06, KAT 08]. Due to its relative simplicity and good performance, this control structure was used in this chapter as the basis for further analysis and development. By treating the last two terms in equation [8.5] as disturbances, the plant that relates the actuator current to the actuator force can be viewed as a simple gain matrix. The actuator force control problem can therefore be represented using the block diagram as shown in Figure 8.6(a). By applying the typical disturbance observer-based control scheme to this system, the resulting closed-loop system is given in Figure 8.6(b). It can be seen in Figure 8.6(b) that the feedback block used in this scenario need only be a gain matrix instead of a low-pass filter as often used in other applications. This is the result of allocating the other dynamical terms as system disturbances to be rejected. Using the proposed controller,

the commanded actuator current can be written as equation [8.8], with K_f being the controller gain used in the feedback path of the disturbance observer, F_c being the vector of commanded force, G being the gain matrix in the forward path and H being the gain matrix in the feedback path. This gain K_f can take on values between zero and 1, and better disturbance rejection can be achieved as the gain approaches unity. The proposed control law can be seen as a simpler version of other similar disturbance observer-based approaches found in the literature as it does not require measurement of actuator velocity or acceleration. This is because the robot inertia matrix and manipulator Jacobians are purely dependent on the configuration of the manipulator end-effector.

$$i_c = \frac{1}{K_t K_a (1-K_f)} D^{-1} F_c - \frac{K_f}{K_t K_a (1-K_f)} D^{-1} F_{act} = \frac{1}{K_t K_a} (GF_c - HF_{act}) \qquad [8.8]$$

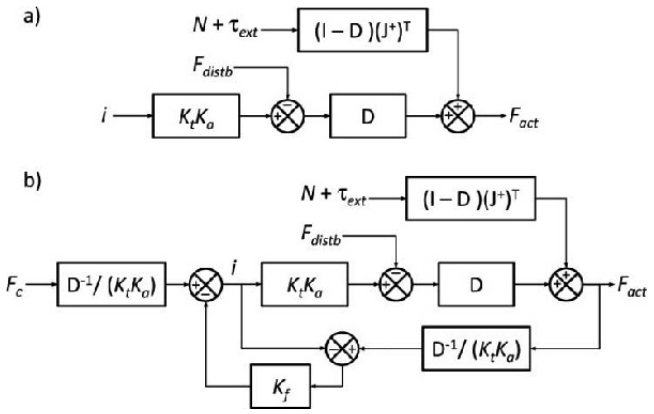

Figure 8.6. *Block diagrams of the actuator dynamics a) and block diagram of the system under disturbance observer-based control b).*

8.3.1.1. *Benefits of decoupling*

Substitution of the control law equation [8.8] into equation [8.5] then yields equation [8.9], which shows no coupling between the commanded force and the actual actuator force. An additional benefit of the application of the decoupling gain matrix can be seen by considering the effect that the control law equation [8.8] has on task space accelerations. One of the fundamental uses of actuator force control is to provide improved backdrivability to the rehabilitation robot. This is equivalent to having a zero vector as the commanded force. Substituting equation [8.8] with zero

commanded force into the original actuator force dynamics equation [8.1] then yields equation [8.10], with F_{distb} being a disturbance force which includes frictional and velocity-dependent components of the actuator dynamics. Combination of equations [8.10] and [8.2] will further lead to equation [8.11], which shows that the effective inertia matrix of the mechanism is dependent on the feedback gain matrix H. It can be shown that the effective inertia matrix in equation [8.11] can be eventually simplified to the form shown in equation [8.12] if H is a multiple of the decoupling matrix D^{-1}, with $m_a = K_a^2 J_{eff}$ and $h = K_f / (1 - K_f)$.

$$F_{act}F_c + (1+K_f)(I-D)(J^+)^T(N+\tau_{ext}) - (1-K_f)DF_{distb} \quad [8.9]$$

$$F_{act} = (I+H)^{-1}[-K_a^2 J_{eff} J\ddot{\Theta} - F_{distb}] \quad [8.10]$$

$$[M + K_a^2 J_{eff} J^T (I+H)^{-1} J]\ddot{\Theta} + N + \tau_{ext} = -J^T (I+H)^{-1} F_{distb} \quad [8.11]$$

$$M + m_a J^T (I+H)^{-1} J = M + \left[\frac{(1+h)}{m_a} V_j \sum_J^{-2} V_J^T + hM^{-1} \right]^{-1} \quad [8.12]$$

Closer inspection of equation [8.12] reveals that the second term on the right-hand side is mainly dominated by the term hM^{-1} if m_a is large, which means that the effective inertia matrix would be very similar to a scaled version of the original manipulator inertia matrix. As a result, provided that the robot inertia matrix is diagonally dominant and has a relatively small condition number (this was found to be the case with the developed robot), externally applied torques will mainly contribute to accelerations along similar directions. Since the externally applied torque represents the interaction between the user and the robot, the above implies that the use of the decoupling matrix in the feedback path will allow more intuitive motion of the robot when the user applies an effort to backdrive the manipulator. On the other hand, if an identity matrix is used in the feedback path, the resulting effective inertia matrix of the controlled manipulator will be heavily influenced by the manipulator Jacobian, in particular when the feedback gain is small. In fact, the condition number of the second term in the effective inertia matrix will be the square of that for the manipulator Jacobian, indicating that coupling will be amplified in general even with relatively well-conditioned manipulator Jacobians.

8.3.1.2. *Generalization of the decoupling force controller*

The control law in equation [8.8] can be further generalized to allow a variation in the level of "decoupling" and the application of additional control action in the null space of the manipulator Jacobian transpose. This modified control law is given in equation [8.13], where n is the power to which the matrix D^{-1} is raised $(0 \le n \le 1)$ and K_{vo} is the gain for the additional disturbance observer applied along the null vector of the manipulator Jacobian. The main rationale for the addition of a disturbance observer loop in the null space is as follows. Since forces along the null space do not influence the task space moments and motion, its control parameters can be chosen independently. Furthermore, in this particular application, the singular value of the matrix D^{-1} along the null vector is significantly lower than that of the other directions due to the large actuator transmission ratio. The result of this is a smaller control action and a corresponding decrease in disturbance rejection capability along the null space. The addition of the disturbance observer in the null space, therefore, aims to compensate for the above shortcoming.

$$i_c = \frac{1}{K_t K_a}\left[\left(\frac{1}{(1-K_f)}D^{-n} + \frac{1}{(1-K_{v0})}v_0 v_0^T\right)F_c - \left(\frac{K_f}{(1-K_f)}D^{-n} + \frac{K_{v0}}{(1-K_{v0})}v_0 v_0^T\right)F_{act}\right] \quad [8.13]$$

The main motivation for the introduction of partial decoupling through variation of the negative power applied to the D matrix is discussed below. Due to the presence of unmodeled dynamics, there exists a limit for K_f above which the system will become unstable. The introduction of partial decoupling, therefore, allows the controller to be further fine-tuned so that the relative gains applied along each decoupled direction can be changed to strike a balance between the disturbance rejection capability and extent of decoupling while maintaining the overall system stability. The above can be illustrated more clearly by considering a simplified problem. By making the assumption that the force control problem can be perfectly decoupled into four single degree of freedom systems (each lying in one of the decoupled directions or output basis vectors of the D matrix), it can be seen that each of these degrees of freedom will have its own gain margin or critical gain. Clearly, the ratios of these gain margins may not be identical to those of the singular values obtained from the decoupling matrix D^{-1}. It is easy to see that a stable system can only be achieved if the effective gains along all the decoupled directions are less than their corresponding critical gains. Since the effective gains along each of these decoupled directions are dependent on both the singular value of D^{-1} along that direction and the overall controller

gain K_f, the restriction of the relative ratios of singular values in H to that found in D^{-1} will generally lead to the case where effective gains along the decoupled directions are not maximized. A possible approach to alleviate this problem is through the introduction of partial decoupling, which provides an additional controller parameter that can be adjusted so that the effective gains can be pushed closer to their critical values while also maintaining some level of decoupling.

8.3.2. *Higher order dynamic model of actuator–sensor–environment system*

Stability of force feedback controllers are often compromised due to the presence of unmodeled dynamics and non-collocation of sensor and actuator [AN 87]. The main implication of this phenomenon is the existence of an upper force feedback gain limit. The higher order dynamics introduced by compliance of the force sensor and actuator must, therefore, be considered for a better understanding of the stability of a force feedback controlled system. Higher order dynamics in the force sensor-based actuator force control problem was modeled in [BUE 06, BUE 07] as a three-mass system with two masses representing the actuator and one mass representing the force sensor. This had been done to describe both the first resonance mode of the actuator and the compliance introduced by the force sensor. By assuming a rigid interface between the force sensor and the interacting mechanical environment, the environmental dynamics can also be integrated into the three-mass model to allow for an analysis on the overall system stability. In this chapter, this combined system is referred to as the actuator–sensor–environment system. It should also be noted that when viewed from the perspective of the actuators, the end-effector dynamics of the parallel manipulator as well as any associated kinematic coupling are considered as part of the environment.

8.3.2.1. *Three-mass model of the actuator and force sensor hardware*

By using a generic three-mass model, the higher order actuator dynamics are found by fitting the actual system into the general model structure. The actual actuator and force sensor hardware used in this research can be modeled as a three-mass system by considering the actuator compliance, sensor compliance and environmental dynamics. Formation of this three-mass model, therefore, requires a more detailed look into the actuator hardware to identify the source of its compliance.

The linear actuators used in this research are powered by brushed DC motors, where the motor torque is transmitted to a ball screw via a 5:1 belt drive. The rotational motion is, in turn, converted into a linear motion through the ball screw with a 3.175 mm (1/8″) pitch. Taking into account the compliance of the belt drive, the vibration mode between the motor and the ball screw is represented graphically in Figure 8.7, where the variables θ, ω, J, r are used to denote angular displacements, angular velocities, rotational inertias and pulley radii respectively. The above variables are also used with subscripts m and s to, respectively, represent quantities relating to the motor and the ball screw. Additionally, k_b and b_b are the stiffness and damping of the transmission belt while b_m and b_s are damping introduced by viscous friction on the motor and ball screw. Finally, K_t, i and τ_{load} are, respectively, used to refer to the motor torque constant, motor current and the load torque applied at the ball screw. Taking the Laplace transform of the motor and ball screw dynamics into account then leads to equations [8.14] and [8.15].

$$[J_m s^2 + (b_m + 2r_m^2 b_b)s + 2r_m^2 k_b]\theta_m(s) = K_t I(s) + 2(r_m r_s b_b s + r_m r_s k_b)\theta_s(s) \quad [8.14]$$

$$[J_s S^s + (b_s + 2r_s^2 b_b)_s + 2r_s^2 k_b]\theta_s(s) = -\tau_{load}(s) + 2(r_m r_s b_b s + r_m r_s k_b)\theta_m(s) \quad [8.15]$$

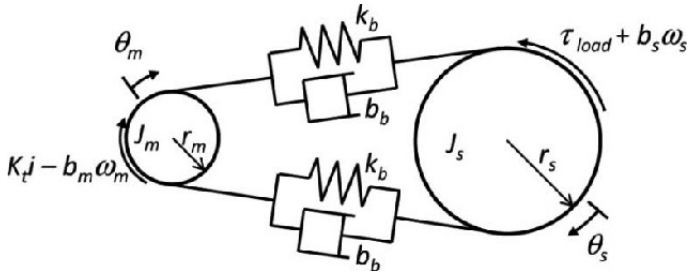

Figure 8.7. *Loading conditions between the motor rotor and the ball screw*

Assuming a perfectly rigid transmission between the ball screw and the linear actuator rod, the belt drive compliance would become the sole source of actuator compliance, thus resulting in a two-mass model for the actuator. Addition of the force sensor onto the end of the actuator rod then results in the setup shown in Figure 8.8, where x_r and x_f are the displacements of the actuator rod and force sensor, $G_s = 2\pi/\text{pitch}$ is the transmission ratio of the ball screw, m_r is the mass of the actuator rod, b_r is the viscous friction acting on the actuator rod and F_{int} is the interaction force between the force sensor

and the environment. Also, m_f, b_f and k_f are the mass, damping and stiffness of the force sensor, respectively. Analysis of the dynamics of this system leads to equations [8.16] and [8.17]. It should be noted that for completeness, a force F_{fric} is also applied onto the rod to represent Coulomb friction. However, this force is neglected in further analysis within this section as the relationship of interest is that between the input current and measured force.

$$[m_r s^2 + (b_r + b_f)s + k_f]X_r(s) = G_s \tau_{load}(s) + (b_f s + k_f)X_f(s) - F_{fric}(s) \quad [8.16]$$

$$[m_f s^2 + b_f s k_f]X_f(s) = -F_{\text{int}}(s) + (b_f s + k_f)X_r(s) \quad [8.17]$$

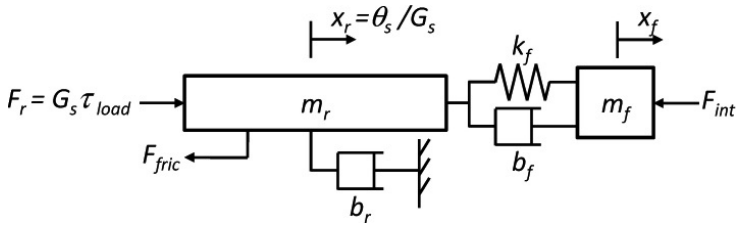

Figure 8.8. *Loading conditions between the actuator rod and the force sensor*

To complete the definition of the actuator–sensor–environment system, the interaction force shown in Figure 8.8 needs to be related to the dynamics of the interacting environment. In reality, this environment would involve the kinematic coupling imposed by the parallel mechanism. However, for the purpose of illustrating the relationship between the actual actuator parameters and the system parameters of the three-mass model given in the previous section, the force sensor is considered to be rigidly coupled to a single degree of freedom environment through a certain transmission ratio as shown in Figure 8.9. The reason for the introduction of this transmission ratio σ is to allow incorporation of the manipulator Jacobian singular values into the unidirectional model. This arrangement basically considers the unidirectional system to be acting along one of the output basis vectors of the manipulator Jacobian, with the transmission ratio being a factor which scales the task space motion to joint space motion. As the motion variable shown in Figure 8.9 is that of the task space displacement, the associated environmental parameters are also given in the task space. The Laplace transform of the environmental dynamics can be written as equation [8.18].

$$\frac{1}{\sigma^2}[m_e s^2 + b_e s + k_e]X_f(s) = F_{\text{int}}(s) \qquad [8.18]$$

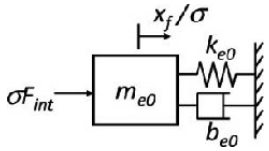

Figure 8.9. *Environment dynamics along one of the output basis vectors of the manipulator Jacobian*

By considering all the dynamic equations above and using the parameterization shown in equation [8.19], the actuator–sensor–environment system can be restated as the three equations shown in equations [8.20]–[8.22].

$$\frac{r_s}{r_m} G_s X_m(s) = \theta_m(s) \qquad [8.19]$$

$$\begin{aligned}&\left[G_s^2 \frac{r_s^2}{r_m^2} J_m s^2 + G_s^2 \left(\frac{r_s^2}{r_m^2} b_m + 2r_s^2 b_b\right) s + 2G_s^2 r_s^2 k_b\right] X_m(s) = \frac{r_s}{r_m} K_t G_s I(s) \\ &+2G_s^2 (r_s^2 b_b s + r_s^2 k_b) X_r(s) \Rightarrow d_m(s) X_m(s) = \frac{r_s}{r_m} K_t G_s I(s) + n_{rm}(s) X_r(s)\end{aligned} \qquad [8.20]$$

$$\begin{aligned}&[(m_r + G_s^2 J_s)s^2 + (b_r + b_f + b_s G_s^2 + 2G_s^2 r_s^2 b_b)_s + k_f + 2G_s^2 r_s^2 k_b] X_r(s) \\ &= 2G_s^2 (r_s^2 b_a s + r_s^2 k_a) X_m(s) + (b_f s + k_f) X_f(s) \Rightarrow d_r(s) X_r(s) \\ &= n_{mr}(s) X_m(s) + n_{fr}(s) X_f(s)\end{aligned} \qquad [8.21]$$

$$\left[\left(m_f + \frac{m_{e0}}{\sigma^2}\right)s^2 + \left(b_f + \frac{b_{e0}}{\sigma^2}\right)s + k_f + \frac{k_{e0}}{\sigma^2}\right] X_f(s) = \left(b_f s + k_f\right) X_f(s) \qquad [8.22]$$

8.3.2.2. *Inclusion of kinematic coupling*

The model of the actuator–sensor–environment system discussed thus far has been restricted to motion along a unidirectional path. The extension of this model to one that can be representative of the actuator force control on the developed parallel mechanism, therefore, requires the incorporation of the manipulator kinematics and dynamics as part of the mechanical environment.

To simplify this task, the manipulator can be linearized about a particular operating point so that the manipulator Jacobian matrix J can be used to relate the task space and joint space motion variables as shown in equation [8.23], where Θ is the task space coordinates and X_f is a vector of force sensor displacements for all the actuating links. The combined dynamics of the manipulator and the task space mechanical environment can also be approximated in a linear form as in equation [8.24], where M_e, B_e and K_e are the inertia, damping and stiffness matrices of the manipulator and task space environment.

$$X_f(s) = J\Theta(s) \qquad [8.23]$$

$$(M_e s^2 + B_e s + K_e)\Theta(s) = J^T F_{\text{int}}(s) \qquad [8.24]$$

Since the matrix J is rectangular with more rows than columns due to the use of a redundantly actuated manipulator, by substituting $\Theta(s) = J^{+}X_f(s)$ into equation [8.24] and pre-multiplying the resulting equation by $(J^{+})^{T}$, equation [8.25] can be obtained. As before, v_0 is used to denote the null space of J^T and superscript + is used to represent the pseudo-inverse operation.

$$[\underbrace{(J^+)^T M_e J^+ s^2}_{M_e'} + \underbrace{(J^+)^T B_e J^+ s}_{B_e'} + \underbrace{(J^+)^T K_e J^+}_{K_e'}]X_f(s) = (I - v_0 v_0^T)F_{\text{int}}(s) \qquad [8.25]$$

To obtain the overall dynamics for all four actuators, equations [8.20] and [8.21] can still be reused with variables X_M, X_r and X_f now being vectors. However, the dynamic equations for the force sensor masses have to be re-evaluated due to the coupling which exists between the task space and joint space motion variables. The force sensor dynamics before consideration of the interaction force exerted by the environment is given by equation [8.26]. Due to the redundant actuation, the joint space motion along the null space of J^T is constrained to be zero (i.e. $v_0^T X_f(s) = 0$). This fact can then be used to produce equation [8.27]. The combination of equations [8.25], [8.26] and [8.27] then results in equation [8.28]. This equation, together with equations [8.20] and [8.21], can be used to fully describe the dynamics of the coupled actuator–sensor–environment system.

$$\begin{aligned}&(m_f s^2 + b_f s + k_f)X_f(s) = -F_{\text{int}}(s) + (b_f s + k_f)X_r(s)\\ &\Rightarrow d_f(s)X_f(s) = -F_{\text{int}}(s) + n_{rf}(s)X_r(s)\end{aligned} \qquad [8.26]$$

$$v_0 v_0^T F_{\text{int}}(s) = n_{rf}(s) v_0 v_0^T X_r(s) \qquad [8.27]$$

$$[(M_e^{'} s^2 + B_2^{'} s + K_e^{'}) + d_f(s) I] X_f(s) = n_{rf}(s)(I - v_0 v_0^T) X_r(s) \qquad [8.28]$$

8.3.3. *State space model of the linearized actuator–sensor–environment system*

A more general approach in analyzing the stability of the overall actuator–sensor–environment system under closed-loop control would be to analyze the roots of its characteristic equation. This can be a difficult task if approached from the consideration of the coupled transfer function matrix. However, when the system is expressed as differential equations in a time domain and formulated as a state space model, solution of the system poles simply becomes an eigenvalue problem for the state transition matrix.

The state space model for the coupled system can be easily formulated from the kinematic and dynamic relationships of the motor, ball screw, force sensor and the parallel manipulator as presented in equations [8.14]–[8.17], [8.23] and [8.24]. It is, therefore, convenient to select the state variables x as the angular displacements and velocities of the motors (θ_{m},), the displacements and velocities of the actuator rod (x_r,) and the displacement and velocity of the task space coordinates (Θ,). The inputs u of this model, on the other hand, are the actuator currents and the effective frictional forces along the actuator rod. Lastly, the outputs y of the system are chosen as the force output of the force sensors. This means that the state space model can be represented in the form shown in equation [8.29], where the state, input and output vectors are, respectively, defined as $x = [\Theta^T x_r^T \theta_m \dot{\Theta}^T \dot{x}_r^T \dot{\theta}_m^T]^T$, $u = [i^T F_{\text{fric}}^T]^T$ and $y = F_{\text{meas}}$.

$$\begin{aligned} \dot{x} &= Ax + Bu \\ y &= Cx \end{aligned} \qquad [8.29]$$

Although the above state space model represents the system exactly as described by the linearized dynamic equations, it is possible that the real system would have additional delays. For instance, the actuator current is assumed to be an ideal input variable in the above model. However, in reality, the current is in fact controlled using a pulse-width modulation-based motor driver. Consequently, discrepancies will exist between the commanded and actual actuator current. This discrepancy can be modeled as a first-order

low-pass filter with unity gain and a small time constant to reflect the fact that such delay is expected to be relatively low. The introduction of this low-pass filter into the above state space model will require the augmentation of the state vector to include additional states which describes the filter dynamics given in equation [8.30], with i_c being the commanded current issued by the actuator force controller.

$$\tau_{LP}\frac{di}{dt}+i=i_c \qquad [8.30]$$

The incorporation of the current dynamics into the above state space model will then result in another state space system with the augmented state vector $x'=[x^T i^T]^T$ and a modified input vector $u'=[i_c^T F_{fric}^T]^T$. This system is represented as equation [8.31], with B_i and B_{fric} being submatrices of the original B matrix which correspond to the current and actuator friction inputs.

$$\dot{x}'=\underbrace{\begin{bmatrix} A & B_i \\ 0_{4\times 22} & -\frac{1}{\tau}I_4 \end{bmatrix}}_{A'}x'+\underbrace{\begin{bmatrix} 0_{22\times 4} & B_{fric} \\ \frac{1}{\tau}I_4 & 0_{4\times 4} \end{bmatrix}}_{B'}u' \quad y=\underbrace{[C \quad 0_{4\times 4}]}_{C'}x' \qquad [8.31]$$

8.3.3.1. *Stability analysis of the coupled actuator–sensor–environment system*

The stability of the coupled actuator–sensor–environment system under closed-loop force feedback can be evaluated by examining the higher order dynamic models. Even though these models were obtained from a linearized system, they can be utilized to give a good indication on the system behavior around its linearization point. One additional point to keep in mind is that while the model consisting of the decoupled transfer functions assumes that environmental stiffness and damping is proportional to the environmental inertia matrix, no such restriction is placed on the state space model. The state space model can, therefore, be used to give a more general analysis of the coupled system. Having stated this, however, the decoupled transfer functions do have an advantage as they can be easily analyzed in the frequency domain to yield gain margins that is expected to be indicative of the actual gain margins when the proportionality assumption is not severely violated. Therefore, this section considers the stability of the closed-loop system using both models.

8.3.3.2. *Stability and robustness analysis in state space*

The decoupled transfer functions can only be used if the damping and stiffness matrices are scaled versions of the inertia matrix or if all these matrices share the same decoupled directions. To study more general environments, a state space model can be used as it does not require the above simplification. The basic state space model considered here is that of the actuator–sensor–environment system with low-pass current filtering as presented in section 8.3.3. Due to the use of a digital controller, the stability of the system is analyzed in discrete time. Again, the c2d Matlab® command was used to convert the continuous state space model into its discrete counterpart given in equation [8.32].

$$\begin{aligned} x'_{k+1} &= A'_z x'_k + B'_z u'_k \\ yk &= C'_z x'_k \end{aligned} \qquad [8.32]$$

To incorporate the effect of the proportional-derivative (PD) control action into the state space system, the dynamics of discrete time PD control must be considered. This dynamic relationship can be expressed using the difference equation [8.33], where backward differentiation is done with k indicating the current sample number. Note that the variable F = y is used to represent the force sensor measurement as outputted from the discrete state space model in equation [8.32] while F^* is the resulting force after application of the unity gain PD filter. To allow its integration into the state space model, an alternative but equivalent difference equation as shown in equation [8.34] can be considered.

$$F_k^* = F_k + \frac{Kd}{T}(F_k - F_{k-1}) \qquad [8.33]$$

$$\begin{aligned} F_{k+1}^* &= \left(1+\frac{Kd}{T}\right)F_{k+1} - \frac{K_d}{T}F_k \\ &= \left(1+\frac{Kd}{T}\right)y_{k+1} - \frac{K_d}{T}y_k \\ &= \left[\left(1+\frac{Kd}{T}\right)C'_z A'_z - \frac{K_d}{T}C'_z\right]x'_k + \left(1+\frac{Kd}{T}\right)C'_z B'_z u'_k \end{aligned} \qquad [8.34]$$

Equation [8.34] shows that additional states of F_k^* can be added to the discrete state space model and that the state transition of this variable is

purely dependent on other states x'_k and inputs u'_k of the current sample. The augmented state space model is represented in equation [8.35].

$$\overbrace{\begin{bmatrix} x'_{k+1} \\ F^*_{k+1} \end{bmatrix}}^{x''_{k+1}} = \overbrace{\begin{bmatrix} A'_z & 0_{26\times4} \\ \left(1+\frac{K_d}{T}\right)C'_zA'_z - \frac{K_d}{T}C'_z & 0_{4\times4} \end{bmatrix}}^{A''_z} \overbrace{\begin{bmatrix} x'_{k+1} \\ F^*_{k+1} \end{bmatrix}}^{x''_k} + \overbrace{\begin{bmatrix} B'_z \\ \left(1+\frac{K_d}{T}\right)C'_zB'_z \end{bmatrix}}^{B''_z} u'k \qquad [8.35]$$

$$\underbrace{F^*_k}_{y'_k} = \underbrace{[0_{4\times26} \quad I_4]}_{C''_z} x''_k$$

When a feedback law with a constant gain matrix K as shown in equation [8.36] is used on the system, the closed-loop difference equation for the system states becomes equation [8.37]. Computing the eigenvalues of the $A''_{z,cl}$ matrix can then reveal the pole locations of the system and stability can be verified if all poles are located within the unit circle on the *z*-plane (i.e. the magnitudes of the poles are all less than one).

$$u'_k = -Ky'_k \qquad [8.36]$$

$$x''_{k+1} = (A''_z - B''_zKC''_z)x''_k = A''_{z,cl}x''_k \qquad [8.37]$$

The above state space model can also be used to test the robust stability of the system when uncertainties are incorporated into the original system model. For the purpose of this analysis, all the uncertainties are assumed to be located in the environment and the actual environmental parameters are taken to be the summation of the nominal parameters with an additional uncertain term. Using the above approach and considering equation [8.26], equation [8.24] can be modified to give equation [8.38], where quantities accented with ~ are used to denote the uncertain terms. The introduction of uncertainties to the task space dynamics can also be graphically represented using the block diagram shown in Figure 8.10.

$$\begin{aligned} &(M_e\tilde{M}_e)\ddot{\Theta} + (B_e + \tilde{B}_e)\dot{\Theta} + (K_e + \tilde{K}_e)\Theta = J^T F_{\text{int}} \\ &\Rightarrow (M_e + m_f J^T J + \tilde{M}_e)\ddot{\Theta} + (B_e + b_f J^T J + \tilde{B}_e)\dot{\Theta} \\ &\quad + (K_e + k_f J^T J + \tilde{K}_e)\Theta = b_f J^T \dot{x}_r + k_f J^T x_r \end{aligned} \qquad [8.38]$$

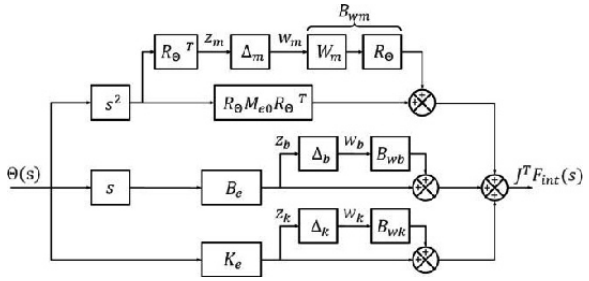

Figure 8.10. *Uncertainty formulation of the task space environment*

It can be seen that the uncertainty terms $\tilde{M}_e$, $\tilde{B}_e$ and $\tilde{K}_e$ in equation [8.38] were, in turn, divided into several blocks in the uncertainty model structure shown in Figure 8.10. The main reason for this was to make the problem more amenable to application of existing robust stability analysis methods. The relationships between the uncertainty matrices in equation [8.38] and the uncertain terms shown in Figure 8.10 are shown in equations [8.39]–[8.41]. It should be noted that in the remaining equations in this section, the terms Δ_m, Δ_b and Δ_k will be referred to as uncertainty matrices while the terms B_{wm}, B_{wb} and B_{wk} will be referred to as uncertainty weighting matrices.

$$\tilde{M}_e = R_\Theta W_m \Delta_m R_\Theta^T = B_{wm} \begin{bmatrix} \delta_{m1} & 0 & 0 \\ 0 & \delta_{m2} & 0 \\ 0 & 0 & \delta_{m3} \end{bmatrix} R_\Theta T \qquad [8.39]$$

$$\tilde{B}_e = B_{wm} \Delta_b B_e \qquad [8.40]$$

$$\tilde{K}_e = B_{wk} \Delta_k K_e \qquad [8.41]$$

It can be seen from equations [8.39]–[8.41] that the method used to model uncertainties in the inertia tensor was slightly different compared to that for the environmental stiffness and damping. By assuming that uncertainties in the environmental inertia tensor only affect values of its principal components and that the principal component axes are aligned with the global reference frame at zero task space coordinates, the inertia uncertainty can be written in the form shown in equation [8.39], with Δ_m being a real diagonal matrix and W_m also a diagonal and real weighting matrix. As less information can be assumed about the environmental stiffness and damping, the uncertainties in these parameters were left in a more general form as shown in equations [8.40]–[8.41], where both the uncertainty matrix and the

uncertainty weighting matrix were general 3×3 complex matrices. Note also that the uncertainties for the stiffness and damping were given in multiplicative terms, as opposed to the additive approach used for the inertia parameter. This means that quantities in the W_m matrix must be selected so that they share the same units as that of the inertia tensor, while B_{wb} and B_{wk} are simply dimensionless weightings.

Robust stability is generally analyzed by first grouping all uncertainty matrices into one block and the remaining closed-loop systems into another block. Using the uncertainty assignment presented in Figure 8.10, the overall closed-loop force control system can be put into such a structure and this is shown in Figure 8.11, where the matrix M_{sys} is used to represent the dynamics of the nominal system under closed-loop force control. This particular form will then allow straight forward application of methods such as small gain theorem and structured singular value analysis for the determination of robust stability.

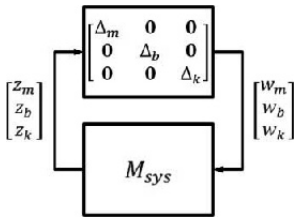

Figure 8.11. *Typical representation of systems with uncertainties where the uncertainty block is separated from the overall system*

The M_{sys} block shown in Figure 8.11 can be obtained by discretizing an extended version of the state space model given in equation [8.31] and closing the loop with the discrete PD force control law. The extension is required to incorporate additional inputs and outputs to M_{sys}. The inputs of M_{sys} are the outputs of the uncertainty matrices $\varepsilon = [w_m^T \; w_b^T \; w_k^T]^T$, while the outputs of M_{sys} are the inputs of the uncertainty matrices $\zeta = [z_m^T \; z_b^T \; z_k^T]^T$. It should be noted that the reason behind the disappearance of the commanded current and PD filtered force measurements (the original inputs and outputs of the state space system) from the input and output ports of M_{sys} was the completion of the force feedback loop within M_{sys}. Extension of the state space model, as described above, has led to the representation of M_{sys} as given in equation [8.42]. Construction of the output and direct feed through matrices ($C_{z\zeta}$ and $D_{z\zeta}$) can be done by considering relationships

$z_m = R_\Theta^T \ddot{\Theta}$, $z_b = B_e \dot{\Theta}$ and $z_k = K_e \Theta$. Additionally, since equation [8.43] is true by definition and equation [8.44] can be obtained from equations [8.38] and [8.43], the continuous input matrix for ε (B_ε) will only have non-zero entries at rows corresponding to $\ddot{\Theta}$.

$$x''_{k+1} = A''_{z,cl} x''_k + \left[\frac{B_{z\varepsilon}}{(1+\frac{K_d}{T}) C'_z B_{z\varepsilon}} \right] \varepsilon k \qquad [8.42]$$
$$\zeta k = C_{z\zeta} x''_k + D_{z\zeta} \varepsilon k$$

$$\tilde{M}_e \ddot{\Theta} + \tilde{B}_e \dot{\Theta} + \tilde{K}_e \Theta = B_{e,\ddot{\Theta}} \varepsilon = [B_{wm}\ B_{wb}\ B_{wk}] \begin{bmatrix} w_m \\ w_b \\ w_k \end{bmatrix} \qquad [8.43]$$

$$\begin{aligned} (M_e + m_f J^T J)\ddot{\Theta} = b_f J^T \dot{x}_r + k_f J^T x_r - (B_e + b_f J^T J)\dot{\Theta} \\ -(K_e - k_f J^T J)\Theta - B_{\varepsilon,\ddot{\Theta}} \varepsilon \end{aligned} \qquad [8.44]$$

The small gain theorem is a relatively simple method of analyzing the robust stability of systems which are expressed in the form shown in Figure 8.11. It states that the closed-loop system shown in Figure 8.11 will be stable as long as the product of the maximum singular value for the uncertainty block and that for M_{sys} is less than one over all frequencies. Typically, the uncertainty weighting is "factorized" out of the uncertainty matrix and included in M_{sys} so that the norm of the uncertainty block can be set to unity. With this condition, the stability of the closed-loop system will be fully reliant on the maximum singular value of M_{sys}. As long as M_{sys} is stable, stability of the closed-loop system will be guaranteed if this maximum singular value is less than one. Although relatively simple to compute, the small gain theorem has the disadvantage of being overly conservative [BAT 02, BUE 05] as it allows all elements in the uncertainty block to take on arbitrary values so long as it satisfies the unity norm condition.

An improved analysis method is the structured singular value, which considers the structure within the uncertainty block. Formally, the structure singular value is defined as equation [8.45] [BAT 02], where μ is the structured singular value, $\tilde{\Delta}$ is the set of uncertainty matrix that satisfies the desired structure and $\sigma_{\max}(\Delta)$ denotes the maximum singular value of Δ. In other words, the structured singular value is inversely related to the size/norm

of the smallest uncertainty matrix Δ (which shares the same structure as $\tilde{\Delta}$) that can cause the system M_{sys} to become unstable by making $\det(I - M_{sys}\Delta) = 0$. On the basis of this definition, a smaller structured singular value indicates higher robust stability. When the uncertainty weightings have been selected to allow a maximum norm of one for Δ, it can be seen that as long as μ is smaller than one, the system will be robustly stable for all possible systems, which falls within the chosen uncertainty bounds. It should be noted, however, that analytical solutions to μ can only be obtained for certain special cases and it is, in general, estimated numerically. The μ function in Matlab® is one such function and it was used in this work.

$$\mu(M_{sys} = \frac{1}{\inf_{\Delta\in\tilde{\Delta}}\{\sigma_{\max}(\Delta)\left|\det(I - M_{sys}\Delta) = 0\right.\}}) \qquad [8.45]$$

As M_{sys} is frequency dependent, computation of the structured singular value will need to be done at all frequencies and the largest result should be returned. To do so, the frequency response of M_{sys} must be obtained. By considering the discrete state space model in equation [8.42], the *z*-transform of ζ can be related to the *z*-transform of ε through equation [8.46]. Since $z = e^{sT}$ and the substitution of s = jω is used to obtain the frequency response of transfer functions, the frequency response $M_{sys}(j\omega)$ is given by equation [8.47].

$$M_{sys}(z) = \frac{\zeta(s)}{\varepsilon(z)} = \left\{ C_{z\zeta}(zI - A''_{z,cl})^{-1}\left[\frac{B_{ze}}{(1+\frac{k_d}{T})C'_z B_{z\varepsilon}}\right] + D_{z\zeta}\right\} \qquad [8.46]$$

$$M_{sys}(j\omega) = \frac{\zeta(j\omega)}{\varepsilon(j\omega)} = \left\{ C_{z\zeta}(e^{j\omega T}I - A''_{z,cl})^{-1}\left[\frac{B_{ze}}{(1+\frac{k_d}{T})C'_z B_{z\varepsilon}}\right] + D_{z\zeta}\right\} \qquad [8.47]$$

The result in equation [8.47] can then be computed on a frequency grid to produce $M_{sys}(j\omega)$ at discrete intervals. This information can then be passed into the μ function to obtain an upper and lower bound on $|\mu(j\omega)|$ over the considered frequencies. The maximum of the upper bound of $|\mu(j\omega)|$ can then be used as an estimate for the structured singular value of M_{sys}. The result of

the structured singular value analysis of the system linearized about the zero task space coordinates is plotted in Figure 8.12 to give an indicative example of $|\mu(j\omega)|$. The highest peak, which is considered to be the structured singular value for M_{sys}, is also marked on the plot. In this chapter, the frequency grid used to compute $M_{sys}(j\omega)$ spans from 10^{-3} to π / T rad/s (the frequency beyond which aliasing will occur in the discrete control system). The final frequency grid used is uniformly spaced on the logarithmic frequency scale with 200 intervals. The choice of the number of intervals was selected by trial and error and is done by gradually decreasing the number of frequency intervals while observing the peak values of $|\mu(j\omega)|$ obtained from the μ function. The smallest number of intervals, which preserves the value of the peaks, was chosen for use in the final analysis. For simplicity, the uncertainty weighting matrices were not chosen to be frequency dependent and were simply selected as scaled identity matrices.

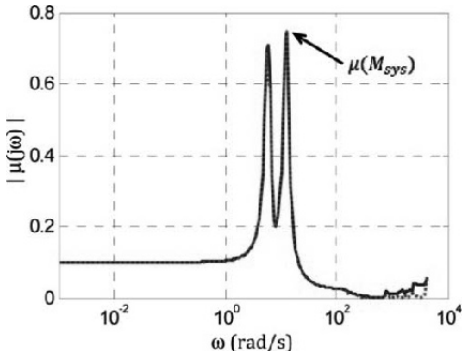

Figure 8.12. *The structured singular values of the system at different frequencies. Solid line indicates the upper bound and dotted line indicates the lower bound*

8.3.4. *Proposed actuator force controller*

On the basis of the above analyses, a gain-scheduled actuator joint force controller was proposed and implemented on the ankle rehabilitation robot as this will give a more optimal performance. The structure of this controller is shown in Figure 8.13, where F_c is a vector of the commanded forces and F_{meas} is a vector of forces as provided by the force sensors. K is the gain matrix, which is given by equation [8.48], where U'_m and v_0 are the output basis

vectors of M_e that can be obtained from the singular value decomposition of M_e. Furthermore, diag(.) is a function that forms a diagonal matrix using its argument and k_i are the controller gains applied to the *i*th basis vector, with i=0 referring to the gain along the null space direction and i=1,2,3 referring to gains along decoupled directions with the first, second and third largest singular values, respectively.

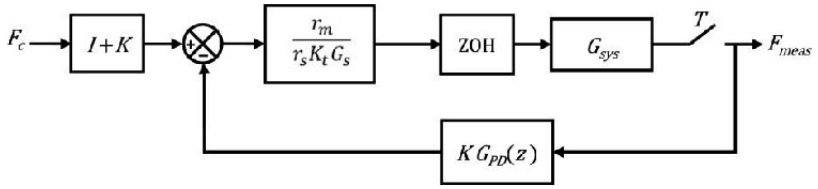

Figure 8.13. *Structure of the final actuator force control law*

$$K = [U_m' \; v_0] diag([k_1 \; k_2 \; k_3 \; k_0])[U_m' \; v_0]^T \qquad [8.48]$$

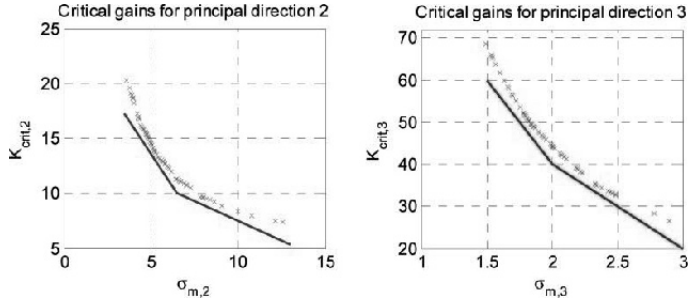

Figure 8.14. *Linear piecewise functions used for gain scheduling in different decoupled directions of M_e'*

Gain scheduling for the controller gains in two of the three non-null decoupled directions was done using piecewise linear functions fitted below the critical gain values. These relationships are shown as solid lines in Figure 8.14, together with the critical gain values for comparison. The remaining non-null direction, on the other hand, was assigned a constant gain since the critical gain variation over the range of singular values considered is relatively small. In addition, as the null direction is not influenced by the configuration of the manipulator, it is assigned a constant gain that is below its gain margin.

A computational ankle model developed in [TSO 10] was used to obtain a more realistic operating environment for the ankle rehabilitation robot. The environmental stiffness experienced during passive ankle motion was estimated from the static torque observed at different ankle and subtalar joint displacements. These torque profiles were then numerically differentiated with respect to the ankle and subtalar displacements to produce the stiffness matrix K_{as}, which is a 2×2 matrix. This matrix was subsequently transformed into the manipulator task space to give a 3×3 stiffness matrix k_e. On the other hand, the environmental damping matrix B_e was assumed to have the form shown in equation [8.49], with both a constant and a variable component. In equation [8.49], b_e is a scalar constant that gives a base level of damping while $\gamma << 1$ is a proportionality constant between the damping and stiffness parameters. The variable component had been included to introduce additional damping in a proportional manner to the ankle stiffness and is mainly used to reduce the damping factor experienced at foot orientations with very high stiffness.

$$B_e = b_e I + \gamma K_e \qquad [8.49]$$

A structured singular value analysis of the proposed actuator force controller was carried out to determine its stability and robustness properties. This analysis was carried out at discrete points in the task space that corresponds to different combinations of ankle and subtalar joint displacements within a certain range (±40° at 4° interval for the ankle displacement and ±30° at 3° interval for the subtalar displacement). At each of these task space coordinates, the environmental stiffness and damping matrices were obtained and used to form the nominal external environment. The uncertainty weighting matrices used in this analysis are given in Table 8.4. The uncertainties considered represent about 5% of the total nominal mass parameter and 10% variations in the stiffness and damping parameters. Note that the environmental mass includes that of the manipulator and as a result of that, 5% uncertainty in the total nominal mass parameters actually relates to a higher proportion (about 10%) of the foot rotational inertia according to estimates derived from [NAS 08].

Uncertainty weighting	B_{wm}	B_{wb}	B_{wk}
Value/expression	$0.002R_\Theta$ kgm^2	$0.1I_3$	$0.1I_3$

Table 8.4. *Uncertainty weighting matrices used in the robust stability analysis*

Stability analysis of the $A''_{z,cl}$ matrix in M_{sys} had shown that all system poles are located within the unit circle on the *z*-plane for the foot configurations tested, thus proving system stability and ensuring that structure singular values can be used to evaluate the robust stability of the system. The results of the structured singular value analyses are summarized in Figure 8.15, where the computed values of $\mu(M_{sys})$ are plotted over their corresponding ankle and subtalar joint displacements. It can be seen in this figure that all the structured singular values are less than one, thus indicating that the system will remain stable as long as the environmental uncertainties remain within the prescribed bounds.

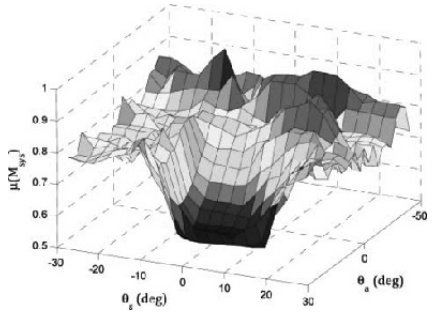

Figure 8.15. *Values of $\mu(M_{sys})$ computed over a range of foot orientations defined by the ankle (θ_a) and subtalar (θ_s) joint displacements*

8.4. Experimental results

Several experimental trials were carried out on the ankle rehabilitation robot developed in this research to evaluate the effectiveness of the proposed actuator force controller. These experiments can be classified into two groups: one to highlight the effects of different force controllers on the system stability and another to evaluate and compare the force control performance of different controllers in executing tasks required by the rehabilitation exercises.

8.4.1. *Stability experiment*

As one of the main motivations behind the development of the proposed force controller is to improve the system stability, one of the experimental trials carried out in this work was centered on demonstrating the stability

improvement brought on through the application of the proposed control scheme. This experimental trial involved the operation of the ankle rehabilitation robot under pure force control, where the force commands were selected by requiring that the vertical component of the null space forces be summed to a desired value to provide support for the user's lower limb, while all remaining non-null space forces are set to be zero. The subject was then prompted to move his or her foot freely in primarily the plantar-/dorsiflexion direction. This experiment was done for four different actuator force controllers, which are listed and described in Table 8.5. The results of this experiment are presented in Figure 8.16. Note that only the forces measured along one of the actuators are shown for brevity, and forces along other directions behave in a similar manner.

Controller	Description
P control, uniform gain of 10	Measured force is fed directly into a disturbance observer, the gain matrix K in [8.48] is obtained by selecting $k_1 = k_2 = k_3 = k_4 = 10$
PD control, uniform gain of 16	Measured force is fed into a disturbance observer through a proportional-derivative filter G_{PD} (z), the gain matrix K in [8.48] is obtained by selecting $k_1 = k_2 = k_3 = k_4 = 16$
Proposed controller	Measured force is fed into a disturbance observer through a proportional-derivative filter G_{PD} (z), the gain matrix K in [8.48] is obtained by observing the gain margins given in Figure 8.14
Proposed controller + minimum gain of 14	Measured force is fed into a disturbance observer through a proportional-derivative filter G_{PD} (z), the gain matrix K in [8.48] is obtained by setting $k_1 = k_0 = 14$, while k_2 and k_3 are obtained by observing the gain margins given in Figure 8.14

Table 8.5. *Actuator force controllers considered in the stability experiments*

From the experiments, motions obtained using the first two controllers showed clear signs of instability with significant levels of oscillation. This is backed up by the actuator force measurements given in Figure 8.16. Since the gains of the uniform gain controllers were selected to be the lowest gains that will result in perceptible oscillations in the robot, it can be seen that the addition of the proportional derivative term in the feedback loop does indeed improve the stability of the system and allow better performance through

application of larger controller gains. Furthermore, Figure 8.16 also shows that although some of the gains applied along certain decoupled directions of the third and fourth controllers considered were larger in value than that of the second uniform gain controller, these controllers remained stable during the operation. This supports the idea that there are directions that are less stable and these directions ultimately limit the maximum gain that can be applied in a controller with uniform gains. Consequently, the important conclusion that can be drawn from this experiment is that when actuators are independently controlled with its own disturbance observer (the uniform gain control approach), the maximum performance achievable would be limited due to the upper gain limit imposed by the system stability. However, when the coupling introduced by the manipulator kinematics and inertia is taken into account, it is possible to manage stability through application of different gains along different decoupled directions of M_e'. This allows higher gains in more stable directions, and thus results in an improved overall performance.

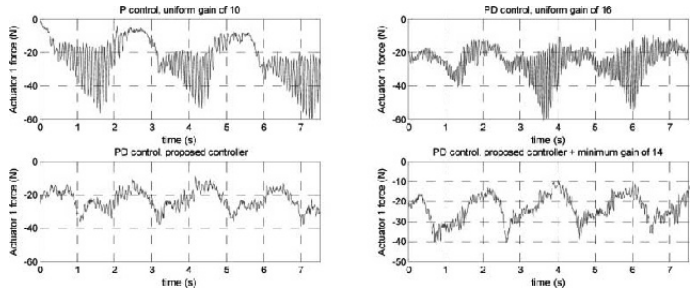

Figure 8.16. *Forces measured along actuator 1 using different actuator force controllers*

8.4.2. *Experiments for performance evaluation*

In addition to the stability experiment, further trials were also carried out using both a uniform gain controller and the proposed controller to illustrate the performance improvements afforded through incorporation of the coupling information into the controller. These experiments were again done on the developed ankle rehabilitation robot and involve two main tasks that are considered important for implementation of ankle rehabilitation exercises and will test the force controllers. The first task is the ability to maximize the backdrivability of the robot by commanding zero task space moments (such as that done in the stability experiment) and the second task is the explicit

control of the robot–user interaction moment. Both tasks were carried out using a uniform gain actuator force controller with a gain of five, and the proposed controller (note that the gain of five is also used along the output basis vector of M_e' which has the largest singular value). The results for the first task described above are summarized in Figure 8.17 and the results obtained from the second task are presented in Figures 8.18 and 8.19.

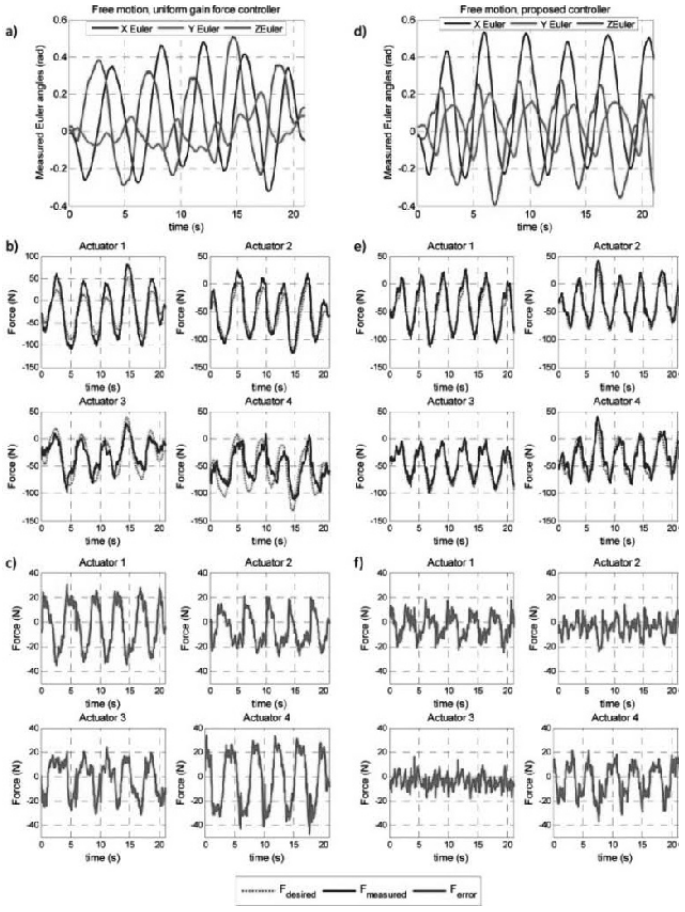

Figure 8.17. *Experimental results obtained during free motion of the user's foot on the ankle rehabilitation robot. The Euler angle trajectories for the uniform gain controller are shown in a) while the associated actuator forces and force errors are given in b) and c). Similarly, the motion trajectories obtained using the proposed controller are given in d) and its associated forces and force errors are shown in e) and f)*

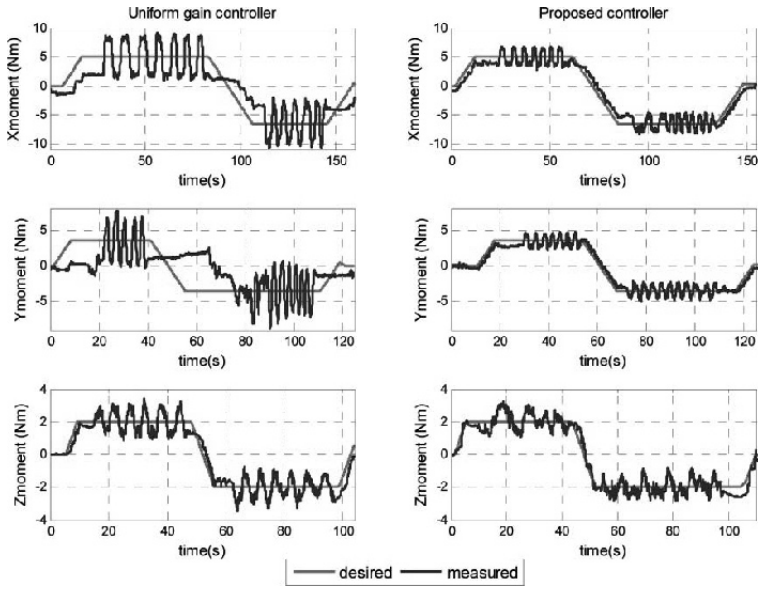

Figure 8.18. *Desired and measured ankle moments about the ankle as obtained from the torque control experiment*

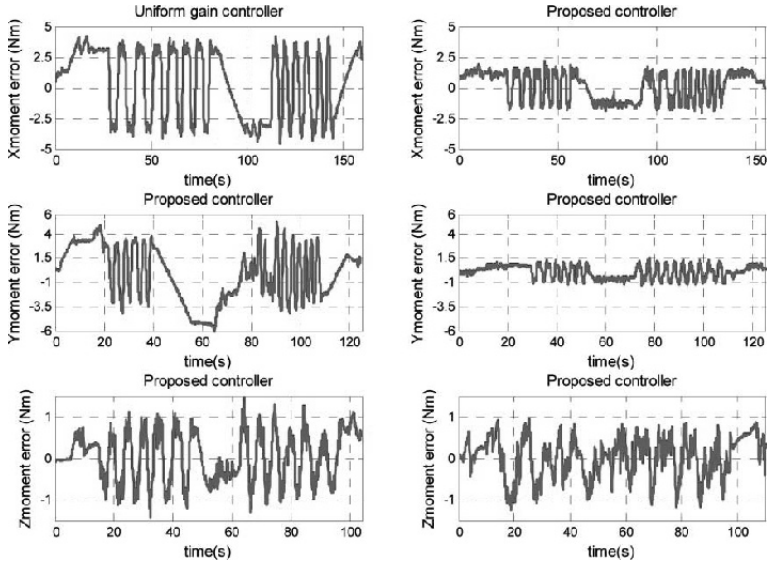

Figure 8.19. *Moment errors as obtained from the torque control experiment*

It can be seen from the results obtained in the free motion trials that utilization of the proposed control scheme over the uniform gain controller can significantly reduce the actuator force errors, with some of the actuators experiencing a force error reduction of about 50%. Comparison of Figures 8.17(a) and (d) also suggests that the force-proposed controller is more capable in terms of maximizing the compliance of the ankle rehabilitation robot since it appears that motion recorded using the proposed controller is of larger amplitudes and velocities relative to that of the uniform gain controller.

Inspection of results from the torque control trials also showed similar trends, where moment tracking capability of the robot is significantly improved in the X and Y directions when the proposed controller is used over the uniform gain controller. The moment performance along the Z-direction, however, is similar between the two controllers. This can be explained by how the task space moments are related to the actuator forces through the manipulator Jacobian transpose J^T. Singular decomposition of J^T can be used to show that the output basis vector of J^T with the most influence on the Z-direction is linked to an input basis vector that is closely aligned with the basis vector of K with the smallest gain. Because this smallest gain is also of the same magnitude as the gain used in the uniform gain controller, it is not surprising that similar moment errors were observed along the *z*-direction. Similarly, the X and Y task space moments can also be found to be more closely linked to the directions where gains k_2 and k_3 are applied in the proposed controller. This further agrees with the observation that smaller moment errors were recorded in the Y-direction.

The results of the torque control trials have suggested that the moment errors are large, even with the use of the proposed controller. It should be noted, however, that this error is mainly caused by frictional effects and does not vary significantly with the amplitude of the commanded torque levels. This is shown in Figure 8.20, where the moment regulation performance of the robot in the X-direction was tested at three different levels. It is clear from the moment error plot that the magnitude of the errors remained relatively constant regardless of the value of the reference moment. This implies that the robot is not capable of realizing the desired moment in a very precise manner. Given that low moment commands are used mainly to improve the robot backdrivability, the above results mean that an effective frictional moment of approximately 1.5 Nm is to be expected on the robot. Although not ideal, this is considered to be acceptable for this application, as the user should be able to easily overcome such resistance. For tasks

involving larger moment commands such as strengthening exercises, the moment error will become less significant and will not severely degrade the performance of the robot.

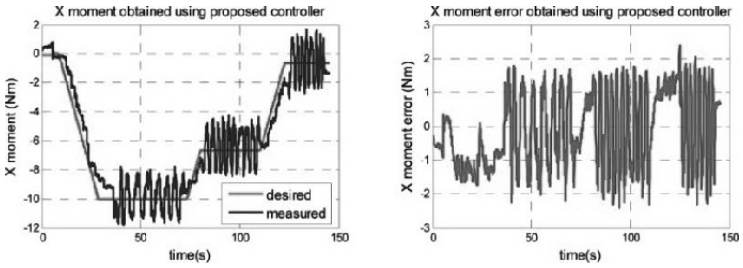

Figure 8.20. *Experimental results obtained by using the proposed controller in regulation of the X interaction moment at three different levels*

8.5. Concluding remarks

This chapter detailed the development of a MIMO actuator force controller for the ankle rehabilitation robot that incorporates the user into the system. The coupling between actuator forces was first identified and an initial design of a disturbance observer-based decoupling force control scheme that considers the kinematic and inertial characteristics of the robot was presented. Although this decoupling control scheme cannot be implemented directly on the robot due to stability issues originating from the presence of unmodeled dynamics, it has provided valuable insights into the coupled force dynamics by highlighting the possibility of transforming the force control problem into a separate force coordinate frame whose bases are spanned by the output basis vectors or decoupled directions of the coupling matrix D.

Using this transformation, further analyses were carried out on a higher order model of the actuator, which includes the actuator and force sensor compliance. By applying certain simplifying assumptions, the force control problem was completely decoupled along these decoupled directions. On the basis of these analyses, an additional proportional derivative filter was included into the disturbance observer and gain margins along these decoupled directions were established for different orientations of the robot end-effector. It was found that the gain margins vary rather significantly among different decoupled directions as well as across different end-effector orientations of the ankle rehabilitation robot. This had led to the proposal of a gain-scheduled MIMO actuator force controller in this research.

Experiments have shown the proposed method to be effective in improving the performance of the force controller over the conventional uniform gain approach (which is also the approach where each actuator is controlled independently from one another). Additionally, as the computed gain margins allow partial decoupling of the actuator–robot system, the condition number of the effective end-effector inertia is also significantly reduced in the proposed control scheme, thus making the backdrivability of the robot more uniform in different directions.

8.6. Bibliography

[ACC 07] ACC, Accident Compensation Corporation, New Zealand, retrieved 24 October 2007. Available at http://www.acc.co.nz/for-providers/resources/WCMZ002647?ssSourceNodeId=4249&ssSourceSiteId=149.

[AN 87] AN C.H., HOLLERBACH J.M., "Dynamic stability issues in force control of manipulators", *IEEE International Conference on Robotics and Automation*, 1987.

[BAT 02] BATES D.G., POSTLETHWAITE I., "The structured singular value and mu-analysis", in FIELDING C., VARGA A., BENNANI S., SELIER M. (eds), *Advanced Techniques for Clearance of Flight Control Laws,* Springer, Berlin, pp. 37–55, 2002.

[BUE 05] BUERGER S.P., Stable, high-force, low impedance robotic actuators for human-interactive machines, PhD Dissertation, MIT, 2005.

[BUE 06] BUERGER S.P., HOGAN N., "Relaxing passivity for human-robot interaction", *IEEE/RSJ International Conference on Intelligent Robots and Systems*, 2006.

[BUE 07] BUERGER S.P., HOGAN N., "Complementary stability and loop shaping for improved human–robot interaction", *IEEE Transactions on Robotics*, vol. 23, no. 2, pp. 232–244, 2007.

[DUL 85] DUL J., JOHNSON G.E., "A kinematic model of the human ankle", *Journal of Biomedical Engineering*, vol. 7, no., pp. 137–143, 1985.

[GIR 01] GIRONE M., BURDEA G., BOUZIT M., *et al.*, "Stewart platform-based system for ankle telerehabilitation", *Autonomous Robots*, vol. 10, pp. 203–212, 2001.

[HAB 06] HABIB M.K., "Mechatronics engineering the evolution, the needs and the challenges", *32nd Annual Conference of IEEE Industrial Electronics Society*, 2006.

[HAB 08] HABIB M.K., "Interdisciplinary mechatronics: problem solving, creative thinking and concurrent design synergy", *International Journal of Mechatronics and Manufacturing Systems*, vol. 1, no. 1, pp. 264–269, 2008.

[HAR 95] HARWIN W.S., RAHMAN T., FOULDS R.A., "A review of design issues in rehabilitation robotics with reference to North American research", *IEEE Transactions on Rehabilitation Engineering*, vol. 3, no. 1, pp. 3–13, 1995.

[HER 02] HERTEL J., "Functional anatomy, pathomechanics, and pathophysiology of lateral ankle instability", *Journal of Athletic Training*, vol. 37, no. 4, pp. 364–375, 2002.

[HES 03] HESSE S., SCHMIDT H., WERNER C., *et al.*, "Upper and lower extremity robotic devices for rehabilitation and for studying motor control", *Current Opinion in Neurology*, vol. 16, pp. 705–710, 2003.

[HOG 87] HOGAN N., "Stable execution of contact tasks using impedance control", *IEEE International Conference on Robotics and Automation*, 1987.

[HOG 05] HOGAN N., BUERGER S.P., "Impedance and interaction control", in KURFESS T. (ed.), *Robotics and Automation Handbook*, CRC Press, New York, 2005.

[INM 76] INMAN V.T., *The Joints of the Ankle*, Williams and Wilkins, Baltimore, 1976.

[ISM 68] ISMAN R.E., INMAN V.T., Anthropometric studies of the human foot and ankle, Technical Report 58, The Laboratory, Biomechanics Laboratory, University of California, San Francisco and Berkeley, p. 33, May 1968.

[KAT 06] KATSURA S., MATSUMOTO Y., OHNISHI K., "Analysis and experimental validation of force bandwidth for force control", *IEEE Transactions on Industrial Electronics*, vol. 53, no. 3, pp. 922–928, 2006.

[KAT 08] KATSURA S., IRIE K., OHISHI K., "Wideband force control by position-acceleration integrated disturbance observer", *IEEE Transactions on Industrial Electronics*, vol. 55 no. 4, pp. 1699–1706, 2008.

[KEA 90] KEARNEY R.E., WEISS P.L., MORIER R., "System identification of human ankle dynamics: intersubject variability and intrasubject reliability", *Clinical Biomechanics*, vol. 5, pp. 205–217, 1990.

[KEM 99] KEMPF C.J., KOBAYASHI S., "Disturbance observer and feedforward design for a high-speed direct-drive positioning table", *IEEE Transactions on Control Systems Technology*, vol. 7 no. 5, pp. 513–526, 1999.

[KON 08] KONG K., TOMIZUKA M., MOON H., *et al.*, "Mechanical design and impedance compensation of SUBAR (Sogang University's Biomedical Assist Robot)", *IEEE/ASME International Conference on Advanced Intelligent Mechatronics*, Xi'an, China, 2008.

[KRE 00] KREBS H.I., VOLPE B.T., AISEN M.L., *et al.*, "Increasing productivity and quality of care: robot-aided neuro-rehabilitation", *Journal of Rehabilitation Research and Development*, vol. 37, no. 6, pp. 639–652, 2000.

[LIN 08] LIN C.-C.K., JU M.-S., CHEN S.-M., *et al.*, "A specialized robot for ankle rehabilitation and evaluation", *Journal of Medical and Biological Engineering*, vol. 28, no. 2, pp. 79–86, 2008.

[LIU 06] LIU G., GAO J., YUE H., *et al.*, "Design and kinematics simulation of parallel robots for ankle rehabilitation", *IEEE International Conference on Mechatronics and Automation*, Luoyang, China, 2006.

[MAT 02] MATTACOLA C.G., DWYER M.K., "Rehabilitation of the ankle after acute sprain or chronic instability", *Journal of Athletic Training*, vol. 37, no. 4, pp. 413–429, 2002.

[MER 06] MERLET J.-P., *Parallel Robots*, Springer, The Netherlands, 2006.

[MIT 03] MITTAL R.K., NAGRATH I.J., *Robotics and Control*, Tata McGraw-Hill Education, New Delhi, 2003.

[MUR 93] MURAKAMI T., YU F., OHNISHI K., "Torque sensorless control in multidegree-of-freedom manipulator", *IEEE Transactions on Industrial Electronics*, vol. 40, no. 2, pp. 259–265, 1993.

[NAS 08] NASA, National Aeronautics and Space Administration, retrieved 14 July 2008. Available at http://msis.jsc.nasa.gov/sections/section03.htm.

[PAR 98] PARENTEAU C.S., VIANO D.C., PETIT P.Y., "Biomechanical properties of human cadaveric ankle-subtalar joints in quasi-static loading", *Journal of Biomechanical Engineering*, vol. 120, pp. 105–111, 1998.

[REI 04] REINKENSMEYER D.J., EMKEN J.L., CRAMER S.C., "Robotics, motor learning, and neurologic recovery", *Annual Review of Biomedical Engineering*, vol. 6, pp. 497–525, 2004.

[RIE 05] RIENER R., FREY M., BERNHARDT M., *et al.*, "Human-centered rehabilitation robotics", *IEEE International Conference on Rehabilitation Robotics*, 2005.

[ROY 07] ROY A., KREBS H.I., PATTERSON S.L., *et al.*, "Measurement of human ankle stiffness using the anklebot", *International Conference on Rehabilitation Robotics*, 2007.

[SAF 99] SAFRAN M.R., ZACHAZEWSKI J.E., BENEDETTI R.S., *et al.*, "Lateral ankle sprains: a comprehensive review part 2: treatment and rehabilitation with an emphasis on the athlete", *Medicine & Science in Sports & Exercise*, vol. 31, no. 7, pp. S438–S447, 1999.

[SAG 09] SAGLIA J.A., TSAGARAKIS N.G., DAI J.S., *et al.*, "A high-performance redundantly actuated mechanism for ankle rehabilitation", *The International Journal of Robotics Research*, vol. 28, no. 9, pp. 1216–1227, 2009.

[SAG 10] SAGLIA J.A., TSAGARAKIS N.G., DAI J.S., *et al.*, "Control strategies for ankle rehabilitation using a high performance ankle exerciser", *IEEE International Conference on Robotics and Automation*, 2010.

[SIE 88] SIEGLER S., CHEN J., SCHNECK C.D., "The three-dimensional kinematics and flexibility characteristics of the human ankle and subtalar joints-part I: kinematics", *Journal of Biomechanical Engineering*, vol. 110, pp. 364–373, 1988.

[SUN 07] SUN J.G., GAO J.Y., ZHANG J.H., *et al.*, "Teaching and playback control system for parallel robot for ankle joint rehabilitation", *IEEE International Conference on Industrial Engineering and Engineering Management*, 2007.

[SYR 08] SYRSELOUDIS C.E., EMIRIS I.Z., "A parallel robot for ankle rehabilitation-evaluation and its design specifications", *IEEE International Conference on Bioinformatics and Bioengineering*, 2008.

[TEJ 00] TEJIMA N., "Rehabilitation robotics: a review", *Advanced Robotics*, vol. 14, no. 7, pp. 551–564, 2000.

[TRU 10] TRUONG D.Q., AHN K.K., NAM D.N.C., *et al.*, "Estimation of bending behavior of an ionic polymer metal composite actuator using a nonlinear black-box model", *International Conference on Control, Automation and Systems* (ICCAS), 2010.

[TSA 99] TSAI L.-W., *Robot Analysis: The Mechanics of Serial and Parallel Manipulators,* John Wiley & Sons, New York, NY, 1999.

[TSO 10] TSOI Y.H., Modelling and adaptive interaction control of a parallel robot for ankle rehabilitation, PhD Thesis, University of Auckland, 2010.

[WAN 04] WANG Y., XIONG Z., DING H., *et al.*, "Nonlinear friction compensation and disturbance observer for a high-speed motion platform", *International Conference on Robotics & Automation*, New Orleans, LA, 2004.

[YIN 05] YING N., KIM W., "Determining dual Euler angles of the ankle complex in vivo using 'flock of birds' electromagnetic tracking device", *Journal of Biomechanical Engineering*, vol. 127, pp. 98–107, 2005.

[YOO 05] YOON J., RYU J., "A novel reconfigurable ankle/foot rehabilitation robot", *IEEE International Conference on Robotics and Automation*, Barcelona, Spain, 2005.

[YOO 06] YOON J., RYU J., LIM K.-B., "Reconfigurable ankle rehabilitation robot for various exercises", *Journal of Robotic Systems*, vol. 22, pp. S15–S33, 2006.